Applied Physics Letters

Synthetic aperture interference light (SAIL) microscopy for high-throughput label-free imaging

Cite as: Appl. Phys. Lett. **119**, 233701 (2021); https://doi.org/10.1063/5.0065628
Submitted: 17 August 2021 • Accepted: 29 November 2021 • Published Online: 08 December 2021

Chenfei Hu, Mikhail E. Kandel, Young Jae Lee, et al.

View Online Export Citation CrossMark

ARTICLES YOU MAY BE INTERESTED IN

Low-frequency acoustic generation and nonreciprocal transmission device
Applied Physics Letters **119**, 233501 (2021); https://doi.org/10.1063/5.0066592

How molecular aggregation affects internal quantum efficiency in organic phosphorescent light-emitting diodes
Applied Physics Letters **119**, 233301 (2021); https://doi.org/10.1063/5.0070606

Electron orbital mapping of $SrTiO_3$ using electron energy-loss spectroscopy
Applied Physics Letters **119**, 232902 (2021); https://doi.org/10.1063/5.0072190

Challenge us.
What are your needs for periodic signal detection?
Watch

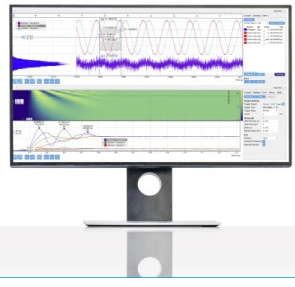

Zurich Instruments

AIP Publishing

© 2021 Author(s).

Applied Physics Letters ARTICLE scitation.org/journal/apl

Synthetic aperture interference light (SAIL) microscopy for high-throughput label-free imaging

Cite as: Appl. Phys. Lett. **119**, 233701 (2021); doi: 10.1063/5.0065628
Submitted: 17 August 2021 · Accepted: 29 November 2021 ·
Published Online: 8 December 2021

View Online Export Citation CrossMark

Chenfei Hu,[1,2] Mikhail E. Kandel,[1,2] Young Jae Lee,[2,3] and Gabriel Popescu[1,2,a)]

AFFILIATIONS

[1]Department of Electrical and Computer Engineering, University of Illinois at Urbana-Champaign, Urbana, Illinois 61801, USA
[2]Beckman Institute for Advanced Science and Technology, University of Illinois at Urbana-Champaign, Urbana, Illinois 61801, USA
[3]Neuroscience Program, University of Illinois at Urbana-Champaign, Urbana, Illinois 61801, USA

[a)]Author to whom correspondence should be addressed: gpopescu@illinois.edu

ABSTRACT

Quantitative phase imaging (QPI) is a valuable label-free modality that has gained significant interest due to its wide potentials, from basic biology to clinical applications. Most existing QPI systems measure microscopic objects via interferometry or nonlinear iterative phase reconstructions from intensity measurements. However, all imaging systems compromise spatial resolution for the field of view and vice versa, i.e., suffer from a limited space bandwidth product. Current solutions to this problem involve computational phase retrieval algorithms, which are time-consuming and often suffer from convergence problems. In this article, we presented synthetic aperture interference light (SAIL) microscopy as a solution for high-resolution, wide field of view QPI. The proposed approach employs low-coherence interferometry to directly measure the optical phase delay under different illumination angles and produces large space-bandwidth product label-free imaging. We validate the performance of SAIL on standard samples and illustrate the biomedical applications on various specimens: pathology slides, entire insects, and dynamic live cells in large cultures. The reconstructed images have a synthetic numeric aperture of 0.45 and a field of view of $2.6 \times 2.6\,\text{mm}^2$. Due to its direct measurement of the phase information, SAIL microscopy does not require long computational time, eliminates data redundancy, and always converges.

Published under an exclusive license by AIP Publishing. https://doi.org/10.1063/5.0065628

Quantitative phase imaging (QPI) is a label-free modality that has emerged as a powerful label-free imaging approach.[1] QPI utilizes the optical phase delay across an object as the contrast mechanism, and thus, it reveals structures of transparent specimens with remarkable sensitivity. Because this modality does not require exogenous labeling, QPI is particularly suitable for nondestructive investigations of biological samples.[2] Optical phase delay is linearly proportional to the non-aqueous content of cells, and thus, it can inform on the cell dry mass, growth, and transport.[3–8] QPI directly reports on the intrinsic biophysical properties of the sample of interest, without artifacts associated with contrast agents. In the past, we have witnessed a broad range of QPI applications in cellular biology,[9–11] cancer pathology,[12–14] tissue disorders,[15–17] neuroscience,[18–20] and materials science.[21–24] More recently, in combination with computational imaging algorithms, QPI enabled tomographic investigations of thin and thick structures,[25–29] while deep learning tools enabled avenues of retrieving chemical specificity from label-free data.[30–33]

The throughput of a conventional QPI system is constrained by the space-bandwidth product (SBP), defined by the range of spatial frequencies within a certain spatial volume.[34,35] Because of this fundamental limit, it is challenging to image a large area with high optical resolution. Although it is generally accepted that the resolution can be improved by using oblique illumination, the factor of enhancement is still limited by the objective numerical aperture, as shown in the supplementary material, Sec. 1 and Ref. 36. Most often, a microscope equipped with a scanning stage is used to accommodate the issue. However, while these instruments are widely spread especially in digital pathology, they require in-focus imaging over large fields of view and some post-processing efforts to align and fuse the individual frames.[37,38] Fourier ptychographic microscopy (FPM) is an alternative solution.[39,40] Instead of fusing the images in the spatial domain, FPM boosts the SBP by scanning and fusing portions of the spatial frequency spectrum. Typically, FPM employs an LED array as the light source, and it records a sequence of intensity images under different

Published under an exclusive license by AIP Publishing

illumination angles. Using a low-power objective to ensure a large field of view (FOV), high-SBP images are produced through computational reconstruction. However, due to the lack of direct phase information, the FPM reconstruction requires an intermediate "phase retrieval" step, which can be time-consuming.[39] Furthermore, fusing the spatial frequency components requires a certain amount of measurement redundancy, i.e., frequency overlap, and nonlinear iterative optimization to retrieve convergent results.[41] A typical FPM uses tens to several hundred input images,[42–44] and the quality of reconstruction is subject to the pattern of illumination,[45,46] sequence of updating,[47] LED misalignment,[48,49] and system noise.[50]

In this article, we present synthetic aperture interference light (SAIL) microscopy as a solution for high-SBP, label-free imaging of micro- and mesoscopic objects. Our imaging system *directly* measures the optical path length map associated with the image field under different angles of illumination, which removes the need for computational phase retrieval algorithms. We applied the synthetic aperture (SA)[51–53] algorithm to generate *deterministic* high-SBP QPI images without iterative optimization. Our reconstructed images have a FOV of $2.6 \times 2.6\,\mathrm{mm}^2$ with a synthetic resolution of $1.45\,\mu\mathrm{m}$, which is approximately $3\times$ better compared to the results without SA reconstruction. In contrast to FPM, SAIL reduces the complexity of the reconstruction and data redundancy, while the results can be computed by a CPU processor in a matter of seconds. Compared to the previous reports of coherent synthesis,[54,55] our instrument is a common path and, thus, robust against temporal phase noise. After the validation on standard samples, we performed measurements on histopathology slides, whole insects, and adherent cell cultures and compared the results with the ones measured by a conventional QPI microscope. This comparison illustrates how hidden structures in conventional imaging can be easily identified in the SAIL reconstruction. We expect that this easy-to-use, high-throughput imaging approach would be of great benefit for biomedical applications in the future.

The general resolution formula for a partially coherent illumination, bright-field microscope, characterized by a condenser numerical aperture, NA_c, and objective numerical aperture, NA_o, is given by $R = 1.22\lambda/(NA_o + NA_c)$. This classical expression may suggest that one can use a low NA_o to achieve large fields of view and a high NA_c for high resolution, which would lead to arbitrary high space-bandwidth products. However, as we show in the supplemental information leading to key Eq. (S16), this resolution formula only applies when $NA_c \leq NA_o$, meaning that the traditional expression for resolution with incoherent illumination should be amended to

$$R = 1.22\frac{\lambda}{NA_o + NA_c}\bigg|_{NA_c \leq NA_o}. \tag{1}$$

Physically, this expression is due to the image formation being the result of the interference between the scattered and incident light. For incoherent illumination, each scattered field only interferes with its own incident field. The incident light acts as a reference of an interferometer, thus amplifying the weak scattering signals (since the camera detects their product). For dark field illumination, the incident field is absent, this amplification mechanism vanishes, and the corresponding scattering fields become negligible compared to those produced by bright field illumination. This is basic phenomenon that motivated the development of synthetic aperture methods, where the scattered light generated by each darkfield illumination plane wave is measured separately and combined numerically. It is important to note that when a plane wave fills the condenser aperture, leading to the light being focused into a spot at the sample, all the plane wave components interfere with each other. As a result, even the dark field illuminated scattered light is amplified by the incident light. Of course, this is the case of laser scanning microscopy, when the resolution is governed by the condenser aperture (typically, another objective), independent of the objective aperture.

In this spirit, we developed the SAIL microscopy instrument to measure the complex image field under various directions of illumination. The optical setup is illustrated in Fig. 1(a). The system is built as an upgrade to an existing differential interference contrast (DIC) microscope, by using a light engine in the illumination path and an interferometric module at the output port. We replaced the conventional halogen lamp with a programmable light engine, consisting of a commercial display projector and a collecting lens group. To precisely control the angle of illumination, we adjusted the position of the light engine such that the projected pattern is focused on the condenser aperture plane. A total of night illumination angles were created. The illumination angles are evenly spaced, with a maximum illumination NA of 0.27. The inset in Fig. 1(a) shows a testing illumination pattern and corresponding image measured at the back focal plane of the microscope objective. At the microscope condenser aperture plane, a Wollaston prism is used to generate two orthogonally polarized illumination beams separated by a small angle, which converts into a small transverse shift at the sample plane. Both beams are incident on the sample and generate scattered light. Using a low magnification microscope objective lens ($5\times/0.15$ NA), only a small angular spread of the scattered light is collected to form the image field. To measure the phase delay between the two sheared beams quantitatively, we removed the analyzer in the conventional DIC microscope and attached a gradient light interference microscope (GLIM) module to the output port. The design principles of GLIM have been discussed in detail in previous publications.[56,57] Briefly, a liquid crystal variable retarder (LCVR) modulates the phase shift between the two image fields, and a subsequent linear polarizer renders the polarization of the two fields parallel. As a result, for a given illumination plane wave, of transverse wavevector $\mathbf{k}_{i\perp}$, the interferogram measured by the detector can be expressed in terms of the irradiance, namely (see the supplementary material, Sect. 2),

$$I(\mathbf{r};\,\mathbf{k}_{i\perp},\varepsilon_n) = |U(\mathbf{r})|^2 + |U(\mathbf{r}+\delta\mathbf{r})|^2 + 2|U(\mathbf{r})U(\mathbf{r}+\delta\mathbf{r})| \times \cos\left[\Delta\varphi(\mathbf{r};\,\mathbf{k}_{i\perp}) + \xi(\mathbf{k}_{i\perp}) + \varepsilon_n\right], \tag{2}$$

where $\mathbf{r}$ is the spatial coordinates; $\mathbf{k}_{i\perp}$ is the transverse wavevector of plane wave illumination; $\varepsilon_n = n\pi/2$ is the phase delay introduced by LCVR; $U(\mathbf{r})$ and $U(\mathbf{r}+\delta\mathbf{r})$ are the image field and its sheared replica, respectively, with $\delta\mathbf{r}$ the shear distance; $\Delta\varphi(\mathbf{r},\mathbf{k}_{i\perp}) = \varphi(\mathbf{r}+\delta\mathbf{r},\mathbf{k}_{i\perp}) - \varphi(\mathbf{r},\mathbf{k}_{i\perp})$ is the phase gradient of interest; and $\xi(\mathbf{k}_{i\perp})$ is the constant phase offset associated with the illumination angle $\mathbf{k}_{i\perp}$. By recording four intensity images, with $n = 0, 1, 2, 3$, a GLIM image can be extracted using phase-shifting interferometry,[1,58] followed by integration along the sheared direction.[59] Detailed discussion about the system calibration and image reconstruction procedure is included in the supplementary material, Secs. 3 and 4. Figures 1(b) and 1(c) show the intensity images and the regular GLIM image of $3\,\mu\mathrm{m}$ polystyrene microspheres. The broadened line profile in Fig. 1(d) indicates that the

Published under an exclusive license by AIP Publishing

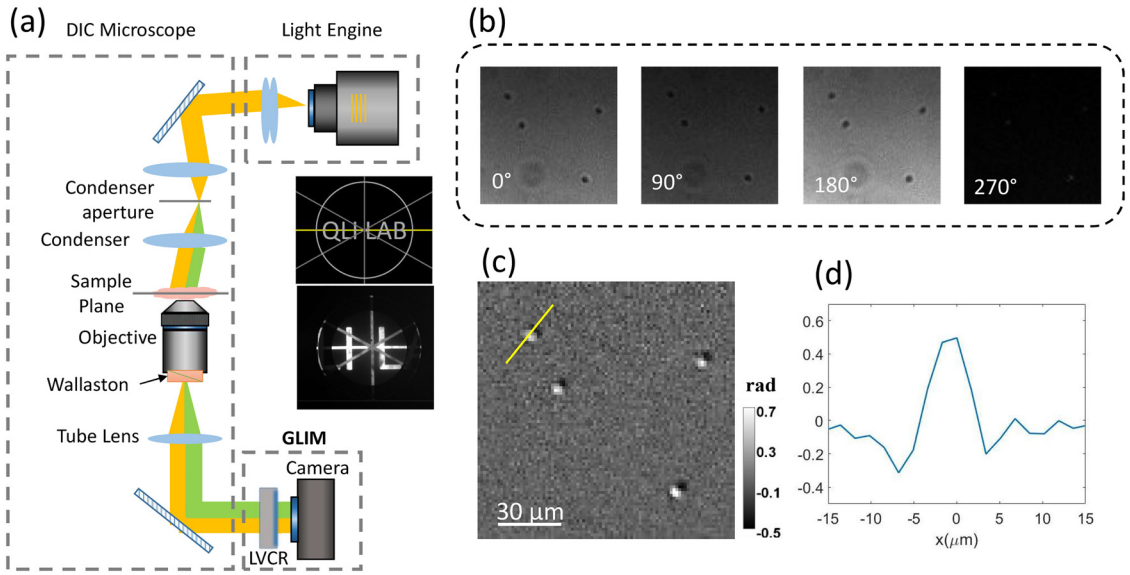

FIG. 1. SAIL system setup and data collection. (a) SAIL microscopy is an upgrade of an existing DIC microscope with a programmable light engine to modulate the angle of illumination and a phase imaging (GLIM) module at the detection port. The light engine is properly aligned such that the projected pattern is focused on the condenser aperture plane. (b) For each illumination angle, 4 intensity images with different phase delays are recorded to retrieve a QPI map. (c) Low-resolution GLIM measurements of 3 μm polystyrene spheres. (d) Due to the resolution limit, the cross section of a bead selected in (c) appears to a broadened profile.

system cannot fully resolve the microspheres. The diffraction-limited resolution of the current setup is approximately 4.27 μm. By alternating the direction of illumination, high-resolution features can be collected SAIL. A detailed description of the system design and data acquisition can be found in the supplementary material, Secs. 5 and 6.

Consider a static weakly scattering object, the propagation of the optical field, U, inside the medium satisfies the inhomogeneous Helmholtz equation,

$$\nabla^2 U(\mathbf{r}) + \beta^2 U(\mathbf{r}) = -\beta_0^2 \chi(\mathbf{r}) U(\mathbf{r}), \tag{3}$$

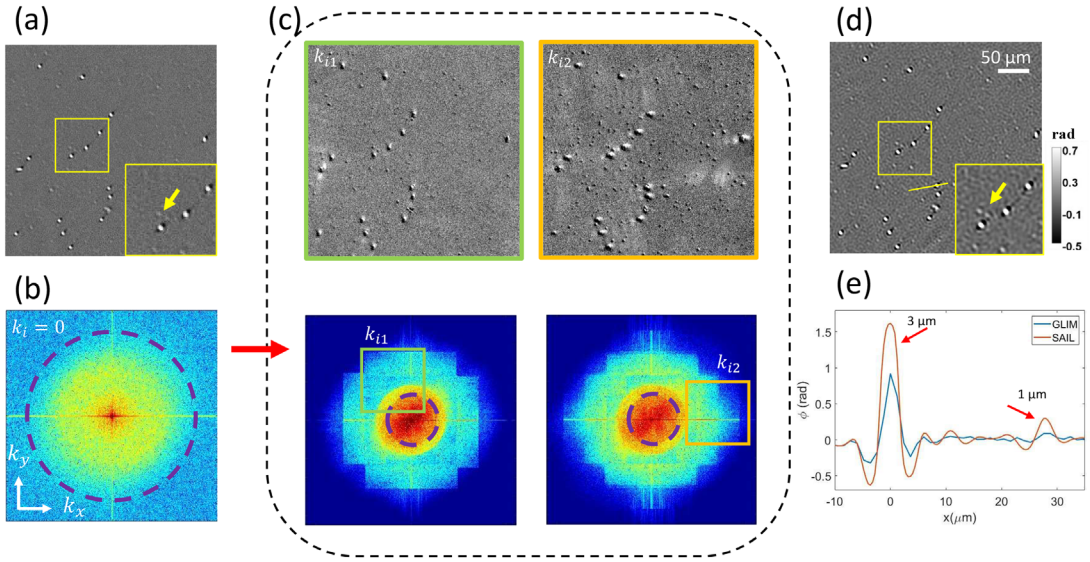

FIG. 2. Principle of the SAIL reconstruction. (a) Using a mixture of 3 and 1 μm polystyrene spheres as a testing object, SAIL reconstruction starts with the phase map corresponding to the central illumination. (b) Taking a 2D Fourier transform of the complex field in (a), the image is brought to the spatial frequency domain. The dashed circle indicates the location of the objective NA. (c) For each measurement with oblique illumination angle, the complex field is also Fourier transformed, and the resulting spectrum is appended to the spectrum in (b). to retrieve a synthetized broad spectrum. (d). Taking an inverse 2D Fourier transform to the synthetized spectrum, a SAIL reconstruction is obtained by extracting the phase of the resulting field. (e) Line profiles of the selected microspheres in (d) before and after SAIL reconstruction.

Published under an exclusive license by AIP Publishing

where $\beta_0 = \omega/c$ is the wavenumber in vacuum; $\beta = n_0\beta_0$, with n_0 the background refractive index; and χ is the object's scattering potential, which essentially provides the image contrast. U is the total field, containing both the incident and scattered light. For a single plane wave incident, the forward scattering field, U_s, collected by an imaging system can be derived from Eq. (3),[60,61] and the solution takes the form (see the supplementary material, Sec. 1 for a derivation)

$$U_s(\mathbf{k}_\perp, z = 0) = A(\mathbf{k}_{i\perp})H(\mathbf{k}_\perp)\chi(\mathbf{k}_\perp - \mathbf{k}_{i\perp}, 0), \tag{4}$$

where $\mathbf{k}_\perp$ is the transverse spatial-frequencies, A is the aperture function of the incident light, and H is the system transfer function. We only consider the object in the focal plane, $z = 0$, and neglect the dependence in the axial direction. Assuming an ideal optical system free of aberration, H can be approximated as a 2D uniform disk with the radius of βNA. Equation (4) states that an illumination field shifts the object's spectrum, and only the frequency components within the system pupil plane are captured to form an image. By employing low-coherence interferometry to capture portions of scattering potential spectrum, synthetic, high-SBP images beyond the conventional limit can be obtained through post-reconstruction.

The principle of SAIL reconstruction is to retrieve synthetic scattering potential, $\widehat{\chi}(\mathbf{k}_\perp)$, by stitching the image spectra measured across all illumination angles. This method, generally referred to as synthetic aperture (SA),[51–53,62] is depicted in Fig. 2. Figure 2(a) shows a mixture of 1 and 3 μm^2 polystyrene microspheres measured at the central illumination, $\mathbf{k}_{i\perp} = 0$. Each SAIL map corresponding to an off-axis illumination angle directly records different portions of the sample's scattering potential. Appending these spectral regions to the regular spectrum ($\mathbf{k}_{i\perp} = 0$), we obtain a synthetic object spectrum [Fig. 2(c)]. By taking a 2D inverse Fourier transform, a SAIL high-SBP image is obtained and its phase extracted, as shown in Fig. 2(d). A detailed description of the reconstruction can be found in the supplementary material, Sec. 7. For the current experimental setup, we achieved a synthetic NA of 0.45, equivalent to 3× enhancement compared to the objective NA. Figure 2(e) compares the cross section of the microspheres measured with and without SA reconstruction.

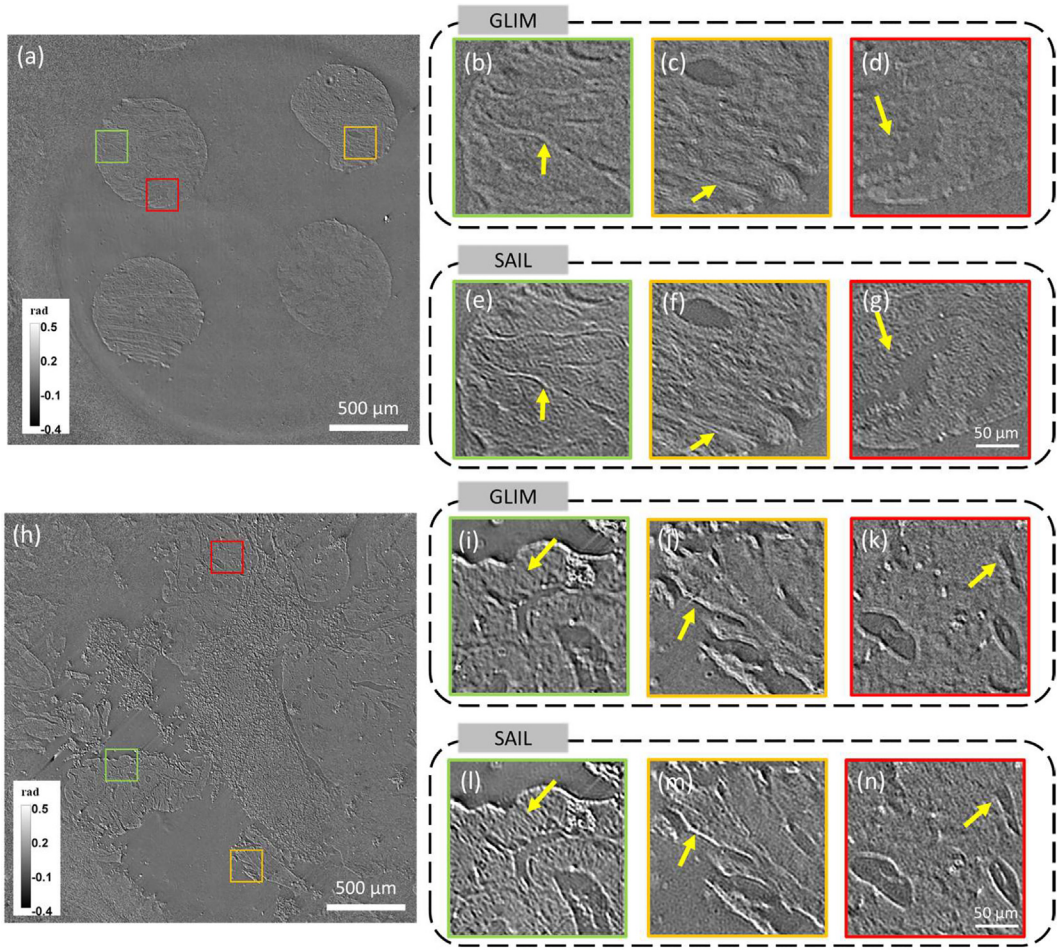

FIG. 3. SAIL imaging of histological specimen. (a) Wide-field low-resolution measurement of a breast tissue microarray, with an imaging area of 2.6 × 2.6 mm^2. (b)–(d) Sub-regions (200 × 200 μm^2) cropped from (a). (e)–(g) SAIL reconstruction cropped at the same region as those in (b)–(d). (h) Wide-field low-resolution image of prostate tissue biopsy. (i)–(k) Sub-regions cropped from (h). (l)–(n) SAIL reconstruction cropped at the same region as those in (i)–(k). As indicated by the yellow arrows, SAIL microscopy reveals tissue structures that cannot be resolved by conventional low-resolution QPI.

Published under an exclusive license by AIP Publishing

Although the synthesized resolution limit cannot resolve features below 1.45 μm, SAIL significantly enhances the sensitivity to the objects below the resolution limit. Compared to existing methods, such as FPM, we measure the complex fields directly, such that the SAIL reconstruction does not require nonlinear iterative optimization to seek convergence, and there is no need to split the FOV into small patches whose areas are on the order of the coherence area.[63,64]

SAIL directly allows screening of histological specimens with high throughput. To illustrate this capability, we performed measurements on unstained histological specimens. A large FOV image of a breast tissue microarray (TMA) and prostate tissue biopsy is shown in Figs. 3(a) and 3(h), respectively. These thin histological samples are approximately 3–4 μm in thickness. The phase values are typically below 1 rad (Refs. 65–67) due to the samples being immersed in xylene and cover-slipped. Using a low-magnification objective, the imaging system directly measures a FOV of $2.6 \times 2.6\,\text{mm}^2$. Figures 3(b)–3(d) and Figs. 3(i)–3(k) show regular inline illumination (GLIM) measurements of tissue portions, while the corresponding SAIL reconstructions at the same sites are displayed in Figs. 3(e)–3(g) and Figs. 3(l)–3(n), respectively. The direct comparison in Fig. 3 shows that SAIL enhances the resolution, where the shape of the tissue gland and fibers in the extra-cellular matrix can be easily identified after the SAIL reconstruction.

SAIL is applicable to high-resolution imaging of mesoscopic organisms without scanning. We tested this performance on several fixed insects. Prepared slides of small insects were purchased from AmScope.[68] These thinly sliced samples were preserved in cedar wood oil and sealed by coverslip. Figure 4(a) shows the wide-field image of female drosophila fixed on a microscope slide. Figures 4(b)–4(d) show regular inline illumination images zoomed in at the costal margin, basal cell, and post-vertical bristles, respectively. The corresponding SAIL reconstructions zoomed in at the same regions are displayed in Figs. 4(e)–4(f). As indicated by the arrows, the computed high-resolution images show the details that cannot be resolved in regular GLIM. In the supplementary material, Fig. S4, we include a similar comparison, where the experiment was performed on a fixed peach worm.

Compared to standard FPM, SAIL microscopy avoids measurement redundancy and provides fast, deterministic reconstruction, with no convergence concerns. Thus, SAIL can be applied to study time-resolved behaviors of large cell populations. To illustrate this potential, live Hela cell cultures were prepared and measured by SAIL microscopy with and without the synthetic aperture. The cells were maintained at room temperature (~21 °C) such that the abnormal incubation condition would inhibit the function of cellular proteins and eventually trigger necrosis.[30] We took one SAIL measurement every 5 min and continuously monitored the cell culture for 3 h. Figure 5(a) shows the SAIL phase image measured at $t = 0$. In Fig. 5(b), we show the inline illumination image of the cropped region shown by the green rectangle in Fig. 5(a) (150×150 μm^2 area) measured at $t = 0$, 1.5, and 3 h, as indicated. The corresponding SAIL images are shown in Fig. 5(c). This time-lapse recording shows the cell volume continuously decreasing, indicating the occurrence of necrosis. Also, the SAIL images reveal structures in the cell bodies, while the cytoplasm appears to be a smooth surface in the regular inline illumination images. A video of these time-lapse measurements can be found in Multimedia View. In the supplementary material, Fig. S5, we show a similar comparison, where the measurements were performed on fixed neuronal culture *in vitro*. Thus, the proposed SAIL microscopy allows large population live-cell screening with high throughput and sensitivity.

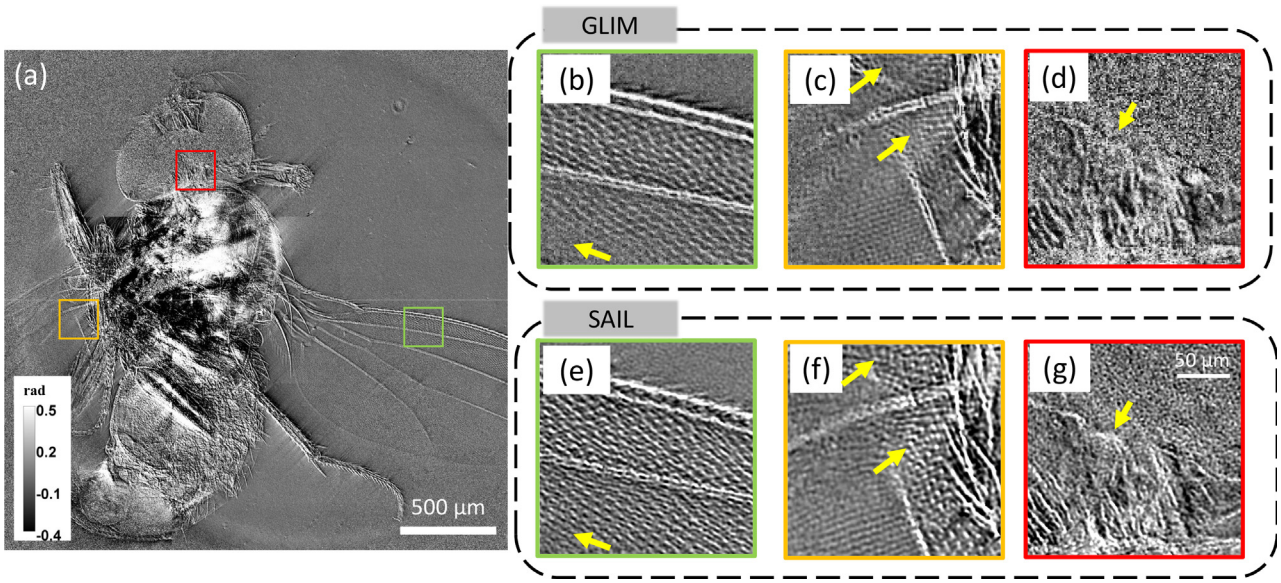

FIG. 4. SAIL imaging of a mesoscopic insect. (a) A wide-field image of female drosophila. (b)–(d) Zoom-in views of costal margin, basal cell, and post-vertical bristles cropped from (a), respectively. (e)–(g) SAIL reconstruction cropped at the same region as those in (b)–(d). The yellow arrows indicate more features of the costal margin, basal cells, and post-vertical bristles can be identified through SAIL reconstruction.

Published under an exclusive license by AIP Publishing

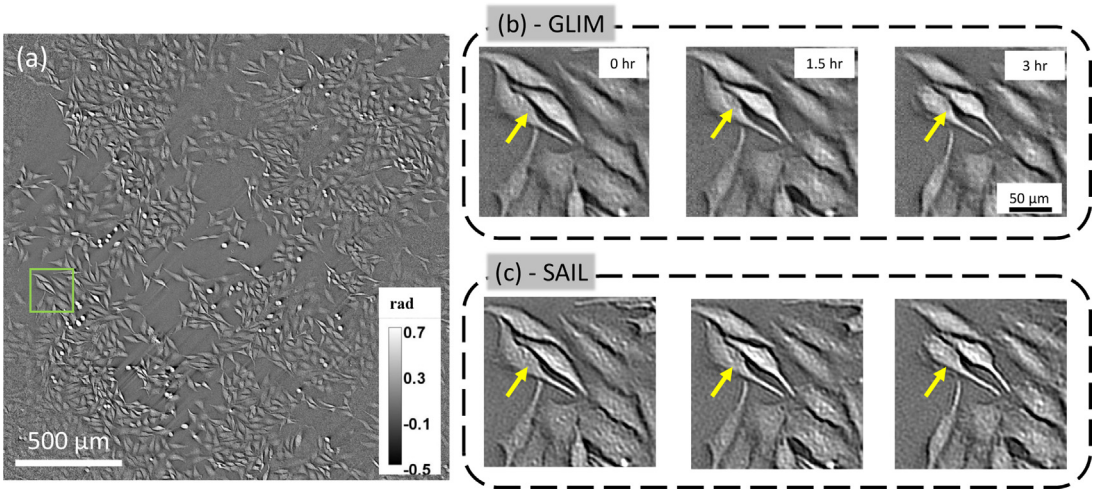

FIG. 5. SAIL imaging of adherent live cells *in vitro*. (a) A wide-field measurement of HeLa cells. (b) Time-lapse GLIM measurements of a sub-region located at the green rectangle in (a), respectively. (c) Time-lapse SAIL reconstruction cropped at the same region as those in (b). A time-lapse video can be found in Multimedia View. The yellow arrows one HeLa appears to be a smooth surface at each time point measured by GLIM, while SAIL shows more features of the cell body. Multimedia View: https://doi.org/10.1063/5.0065628.1

We demonstrated SAIL microscopy to achieve high SBP imaging on mesoscopic transparent specimens. The optical system upgrades an existing QPI microscope by employing a light engine to record the quantitative phase delay under different angles of illumination. By applying the SA reconstruction to synthesize image information, we produce high-resolution QPI results while maintaining a large FOV. Our experimental validation shows that SAIL microscopy enables high-resolution imaging of histological slides, mesoscopic organisms, and cells *in vitro* without scanning or iterative nonlinear reconstruction.

Compared to existing methods that generate high-SBP QPI results by iterative reconstruction from intensity measurements, SAIL produces results with rapid phase retrieval and low redundancy. Because the interferometric module directly measures the phase delay across the FOV, the reconstruction procedure avoids the step of iterative phase retrieval and avoids splitting the FOV into small patches. Furthermore, as each QPI map is an independent measurement of the object's Fourier spectrum, the SAIL reconstruction does not require significant spectrum overlapping between adjacent measurements. On the other hand, in difference to previously demonstrated coherent aperture synthesis approaches,[52,69] SAIL utilizes a common-path interferometry, and the imaging module can be easily added to an existing microscope. Such a system design improves temporal stability and simplifies the procedure of installation and alignment.[1]

The current SA reconstruction scheme assumes an ideal optical system free of aberration. By adapting aberration estimation algorithms[70–73] into the reconstruction framework, we envision that aberration-corrected, high-quality images can be applied to SAIL. Because most of the aberration correction algorithms are iterative, a longer computational time will be needed. Potentially, more efficient, real-time reconstruction would be possible by transferring the processing onto the video card or applying a deep neural network. On the other hand, the complexity of the microscope alignment could be further simplified by replacing the light engine with a liquid crystal module inserted at the condenser aperture plane. In summary, we expect that this label-free, high-throughput imaging modality would be widely used for biomedical research and applications, whenever large areas are studied with high resolution.

See the supplementary material for SAIL system configuration, operation and calibration procedure, and related theoretical derivation.

This work was sponsored in part by the National Institutes of Health (Nos. R01CA238191 and R01GM129709). C.H was supported by the National Institutes of Health (No. T32EB019944).

AUTHOR DECLARATIONS

Conflict of Interest

G.P. has a financial interest in Phi Optics, a company developing quantitative phase imaging technology for materials and life science applications, which, however, did not sponsor the research. The authors disclosed this invention to the Office of Technology Management at the University of Illinois at Urbana-Champaign.

Author Contributions

C.H. built the optical system, developed the reconstruction algorithm, collected the data, performed reconstruction and analysis, and prepared the figures. M.E.K developed the control software. Y.L. prepared HeLa and neuronal cell culture. C.H. and G.P. wrote the manuscript, and G.P. supervised the project.

DATA AVAILABILITY

The data that support the findings of this study are available from the corresponding author upon reasonable request. SA reconstruction script with an example dataset is available for download via https://uillinoisedu-my.sharepoint.com/:u:/g/personal/chenfei3_illinois_edu/Ec1SZc8mkuRGqLaFl0qFH1QBSNXECHih4R4lg5gGRAhhDA?e=UM0O8y.

Published under an exclusive license by AIP Publishing

REFERENCES

[1]G. Popescu, *Quantitative Phase Imaging of Cells and Tissues* (McGraw-Hill, New York, 2011), p. 362.
[2]Y. Park, C. Depeursinge, and G. Popescu, "Quantitative phase imaging in biomedicine," Nat. Photonics **12**(10), 578–589 (2018) (in English).
[3]C. Hu, R. Sam, M. Shan *et al.*, "Optical excitation and detection of neuronal activity," J. Biophotonics **12**(3), e201800269 (2019).
[4]M. Mir, Z. Wang, Z. Shen *et al.*, "Optical measurement of cycle-dependent cell growth," Proc. Natl. Acad. Sci. U. S. A. **108**(32), 13124–13129 (2011) (in English).
[5]D. Huang, I. J. Roy, G. F. Murray, J. Reed, T. A. Zangle, and M. A. Teitell, "Identifying fates of cancer cells exposed to mitotic inhibitors by quantitative phase imaging," Analyst **145**(1), 97–106 (2019).
[6]B. Kemper, A. Bauwens, A. Vollmer *et al.*, "Label-free quantitative cell division monitoring of endothelial cells by digital holographic microscopy," J. Biomed. Opt. **15**(3), 036009 (2010).
[7]H. G. Davies and M. H. F. Wilkins, "Interference microscopy and mass determination," Nature **169**(4300), 541–541 (1952) (in English).
[8]A. E. Vasdekis, H. Alanazi, A. M. Silverman *et al.*, "Eliciting the Impacts of Cellular Noise on Metabolic Trade-Offs by Quantitative Mass Imaging," (in English), Nat Commun **10**, 848 (2019).
[9]Y. Park, M. Diez-Silva, G. Popescu *et al.*, "Refractive index maps and membrane dynamics of human red blood cells parasitized by *Plasmodium falciparum*," Proc. Natl. Acad. Sci. U. S. A. **105**(37), 13730–13735 (2008).
[10]W. J. Eldridge, Z. A. Steelman, B. Loomis, and A. Wax, "Optical phase measurements of disorder strength link microstructure to cell stiffness," Biophys. J. **112**(4), 692–702 (2017).
[11]B. Kemper, S. Kosmeier, P. Langehanenberg *et al.*, "Integral refractive index determination of living suspension cells by multifocus digital holographic phase contrast microscopy," J. Biomed. Opt. **12**(5), 054009 (2007).
[12]H. Majeed, C. Okoro, A. Kajdacsy-Balla, K. C. Toussaint, Jr., and G. Popescu, "Quantifying collagen fiber orientation in breast cancer using quantitative phase imaging," J. Biomed. Opt. **22**(4), 46004 (2017).
[13]S. Sridharan, V. Macias, K. Tangella *et al.*, "Prediction of prostate cancer recurrence using quantitative phase imaging: Validation on a general population," Sci. Rep. **6**, 33818 (2016) (in English).
[14]M. Fanous, A. Keikhosravi, A. Kajdacsy-Balla, K. W. Eliceiri, and G. Popescu, "Quantitative phase imaging of stromal prognostic markers in pancreatic ductal adenocarcinoma," Biomed. Opt. Express **11**(3), 1354–1364 (2020).
[15]C. Hu, M. Santi, O. Adelaja, A. Kajdacsy-Balla, G. Popescu, and W. Kobak, "Imaging collagen properties in the uterosacral ligaments of women with pelvic organ prolapse using spatial light interference microscopy (slim)," Front. Phys. **7**, 72 (2019).
[16]M. Lee, E. Lee, J. Jung *et al.*, "Label-free optical quantification of structural alterations in Alzheimer's disease," Sci. Rep. **6**, 31034 (2016).
[17]M. Schnell, S. Gupta, T. P. Wrobel, M. G. Drage, R. Bhargava, and P. S. Carney, "High-resolution label-free imaging of tissue morphology with confocal phase microscopy," Optica **7**(9), 1173–1180 (2020) (in English).
[18]C. Hu and G. Popescu, "Quantitative phase imaging (QPI) in neuroscience," IEEE J. Sel. Top. Quantum Electron. **24**, 1–1 (2018).
[19]M. Mir, T. Kim, A. Majumder *et al.*, "Label-free characterization of emerging human neuronal networks," Sci. Rep. **4**, 4434 (2014).
[20]S. Pradeep, T. Tasnim, H. Zhang, and T. A. Zangle, "Simultaneous measurement of neurite and neural body mass accumulation via quantitative phase imaging," Analyst **146**(4), 1361–1368 (2021).
[21]B. S. Kim, M. K. Kim, Y. Cho *et al.*, "Electrothermal soft manipulator enabling safe transport and handling of thin cell/tissue sheets and bioelectronic devices," Sci. Adv. **6**(42), eabc5630 (2020).
[22]R. J. Zhou, C. Edwards, A. Arbabi, G. Popescu, and L. L. Goddard, "Detecting 20 nm wide defects in large area nanopatterns using optical interferometric microscopy," Nano Lett. **13**(8), 3716–3721 (2013) (in English).
[23]G. Goetz, T. Ling, T. Gupta *et al.*, "Interferometric mapping of material properties using thermal perturbation," Proc. Natl. Acad. Sci. U. S. A. **115**(11), E2499–E2508 (2018) (in English).
[24]C. Polonschii, M. Gheorghiu, S. David *et al.*, "High-resolution impedance mapping using electrically activated quantitative phase imaging," Light: Sci. Appl. **10**(1), 20 (2021) (in English).
[25]K. Kim, H. Yoon, M. Diez-Silva, M. Dao, R. R. Dasari, and Y. Park, "High-resolution three-dimensional imaging of red blood cells parasitized by plasmodium falciparum and in situ hemozoin crystals using optical diffraction tomography," J. Biomed. Opt. **19**, 011005 (2014) (in English).
[26]C. F. Hu, J. J. Field, V. Kelkar *et al.*, "Harmonic optical tomography of nonlinear structures," Nat. Photonics **14**(9), 564 (2020) (in English).
[27]P. Ledwig and F. E. Robles, "Quantitative 3D refractive index tomography of opaque samples in epi-mode," Optica **8**(1), 6–14 (2021) (in English).
[28]S. Chowdhury, M. Chen, R. Eckert *et al.*, "High-resolution 3D refractive index microscopy of multiple-scattering samples from intensity images," Optica **6**(9), 1211–1219 (2019).
[29]X. Chen, M. E. Kandel, C. F. Hu, Y. J. Lee, and G. Popescu, "Wolf phase tomography (WPT) of transparent structures using partially coherent illumination," Light: Sci. Appl. **9**(1), 142 (2020) (in English).
[30]C. Hu, S. He, Y. J. Lee *et al.*, "Label-free cell viability assay using phase imaging with computational specificity," bioRxiv, 2020.
[31]M. E. Kandel, Y. R. He, Y. J. Lee *et al.*, "Phase imaging with computational specificity (PICS) for measuring dry mass changes in sub-cellular compartments," Nat. Commun. **11**(1), 6256 (2020).
[32]Y. Rivenson, H. Wang, Z. Wei *et al.*, "Virtual histological staining of unlabelled tissue-autofluorescence images via deep learning," Nat. Biomed. Eng. **3**(6), 466–477 (2019).
[33]Y. Jo, H. Cho, S. Y. Lee *et al.*, "Quantitative phase imaging and artificial intelligence: A review," IEEE J. Sel. Top. Quantum Electron. **25**(1), 1 (2019) (in English).
[34]A. W. Lohmann, R. G. Dorsch, D. Mendlovic, Z. Zalevsky, and C. Ferreira, "Space–bandwidth product of optical signals and systems," J. Opt. Soc. Am. A **13**(3), 470–473 (1996).
[35]M. A. Neifeld, "Information, resolution, and space–bandwidth product," Opt. Lett. **23**(18), 1477–1479 (1998).
[36]K. Wicker and R. Heintzmann, "Resolving a misconception about structured illumination," Nat. Photonics **8**(5), 342–344 (2014) (in English).
[37]M. E. Kandel, S. Sridharan, J. Liang *et al.*, "Label-free tissue scanner for colorectal cancer screening," J. Biomed. Opt. **22**(6), 66016 (2017).
[38]M. Fanous, C. Shi, M. P. Caputo, L. A. Rund, R. W. Johnson, T. Das, M. J. Kuchan, N. Sobh, and G. Popescu, "Label-free screening of brain tissue myelin content using phase imaging with computational specificity (PICS)," APL Photonics **6**, 076103 (2021).
[39]G. A. Zheng, R. Horstmeyer, and C. H. Yang, "Wide-field, high-resolution fourier ptychographic microscopy," Nat. Photonics **7**(9), 739–745 (2013) (in English).
[40]A. Pan, C. Zuo, and B. Yao, "High-resolution and large field-of-view fourier ptychographic microscopy and its applications in biomedicine," Rep. Prog. Phys. **83**(9), 096101 (2020).
[41]P. C. Konda, L. Loetgering, K. C. Zhou, S. Xu, A. R. Harvey, and R. Horstmeyer, "Fourier ptychography: Current applications and future promises," Opt Express **28**(7), 9603–9630 (2020).
[42]L. Tian, Z. J. Liu, L. H. Yeh, M. Chen, J. S. Zhong, and L. Waller, "Computational illumination for high-speed *in vitro* Fourier ptychographic microscopy," Optica **2**(10), 904–911 (2015) (in English).
[43]X. Z. Ou, R. Horstmeyer, C. H. Yang, and G. A. Zheng, "Quantitative phase imaging via fourier ptychographic microscopy," Opt. Lett. **38**(22), 4845–4848 (2013) (in English).
[44]A. Pan, Y. Zhang, K. Wen *et al.*, "Subwavelength resolution fourier ptychography with hemispherical digital condensers," Opt. Express **26**(18), 23119–23131 (2018).
[45]J. Sun, Q. Chen, Y. Zhang, and C. Zuo, "Sampling criteria for fourier ptychographic microscopy in object space and frequency space," Opt. Express **24**(14), 15765–15781 (2016).
[46]J. Sun, C. Zuo, J. Zhang, Y. Fan, and Q. Chen, "High-speed Fourier ptychographic microscopy based on programmable annular illuminations," Sci. Rep. **8**(1), 7669 (2018).
[47]K. Guo, S. Dong, P. Nanda, and G. Zheng, "Optimization of sampling pattern and the design of fourier ptychographic illuminator," Opt. Express **23**(5), 6171–6180 (2015).
[48]J. Sun, Q. Chen, Y. Zhang, and C. Zuo, "Efficient positional misalignment correction method for fourier ptychographic microscopy," Biomed. Opt. Express **7**(4), 1336–1350 (2016).

Published under an exclusive license by AIP Publishing

[49]R. Eckert, Z. F. Phillips, and L. Waller, "Efficient illumination angle self-calibration in Fourier ptychography," Appl. Opt. **57**(19), 5434–5442 (2018).
[50]G. Zheng, *Fourier Ptychographic Imaging a Matlab Tutorial* (Morgan & Claypool Publishers, San Rafael, 2016), p. 96.
[51]T. S. Ralston, D. L. Marks, P. S. Carney, and S. A. Boppart, "Interferometric synthetic aperture microscopy," Nat. Phys. **3**(2), 129–134 (2007).
[52]M. Kim, Y. Choi, C. Fang-Yen *et al.*, "High-speed synthetic aperture microscopy for live cell imaging," Opt. Lett. **36**(2), 148–150 (2011).
[53]A. Moreira, P. Prats-Iraola, M. Younis, G. Krieger, I. Hajnsek, and K. P. Papathanassiou, "A tutorial on synthetic aperture radar," IEEE Geosci. Rem. Sens. M **1**(1), 6–43 (2013) (in English).
[54]T. S. Ralston, D. L. Marks, P. S. Carney, and S. A. Boppart, "Real-time interferometric synthetic aperture microscopy," Opt. Express **16**(4), 2555–2569 (2008).
[55]N. Lue, W. Choi, G. Popescu, K. Badizadegan, R. R. Dasari, and M. S. Feld, "Synthetic aperture tomographic phase microscopy for 3D imaging of live cells in translational motion," Opt. Express **16**(20), 16240–16246 (2008).
[56]T. H. Nguyen, M. E. Kandel, M. Rubessa, M. B. Wheeler, and G. Popescu, "Gradient light interference microscopy for 3D imaging of unlabeled specimens," Nat. Commun. **8**, 210 (2017) (in English).
[57]M. E. Kandel, C. Hu, G. N. Kouzehgarani *et al.*, "Epi-illumination gradient light interference microscopy for imaging opaque structures," Nat. Commun. **10**(1), 4691 (2019).
[58]C. Hu and G. Popescu, *Quantitative Phase Imaging: Principles and Applications*, in Label-Free Super-Resolution Microscopy (Springer, 2019), pp. 1–24.
[59]M. R. Arnison, C. J. Cogswell, N. I. Smith, P. W. Fekete, and K. G. Larkin, "Using the Hilbert transform for 3D visualization of differential interference contrast microscope images," J. Microsc. **199**, 79–84 (2000) (in English).
[60]R. J. Zhou, T. Kim, L. L. Goddard, and G. Popescu, "Inverse scattering solutions using low-coherence light," Opt. Lett. **39**(15), 4494–4497 (2014) (in English).
[61]C. Hu and G. Popescu, "Physical significance of backscattering phase measurements," Opt. Lett. **42**(22), 4643–4646 (2017).
[62]W. Luo, A. Greenbaum, Y. B. Zhang, and A. Ozcan, "Synthetic aperture-based on-chip microscopy," Light: Sci. Appl. **4**, e61 (2015) (in English).
[63]G. A. Zheng, R. Horstmeyer, and C. H. Yang, "Wide-field, high-resolution Fourier ptychographic microscopy," Nat. Photonics **9**(9), 621–621 (2015) (in English).
[64]L. Tian, X. Li, K. Ramchandran, and L. Waller, "Multiplexed coded illumination for Fourier ptychography with an LED array microscope," Biomed. Opt Express **5**(7), 2376–2389 (2014) (in English).
[65]M. Takabayashi, H. Majeed, A. Kajdacsy-Balla, and G. Popescu, "Disorder strength measured by quantitative phase imaging as intrinsic cancer marker in fixed tissue biopsies," PLoS One **13**(3), e0194320 (2018).
[66]H. Majeed, S. Sridharan, M. Mir *et al.*, "Quantitative phase imaging for medical diagnosis," J. Biophotonics **10**(2), 177–205 (2017).
[67]S. Sridharan, V. Macias, K. Tangella, A. Kajdacsy-Balla, and G. Popescu, "Prediction of prostate cancer recurrence using quantitative phase imaging," Sci. Rep. **5**, 9976 (2015) (in English).
[68]See https://amscope.com/collections/microscope-parts-accessories-microscope-slides-prepared-microscope-slides/products/ps100a for AmScope.
[69]T. Gutzler, T. R. Hillman, S. A. Alexandrov, and D. D. Sampson, "Coherent aperture-synthesis, wide-field, high-resolution holographic microscopy of biological tissue," Opt. Lett. **35**(8), 1136–1138 (2010).
[70]X. Ou, G. Zheng, and C. Yang, "Embedded pupil function recovery for fourier ptychographic microscopy: Erratum," Opt. Express **23**(26), 33027 (2015).
[71]C. Hu, S. Zhu, L. Gao, and G. Popescu, "Endoscopic diffraction phase microscopy," Opt. Lett. **43**(14), 3373–3376 (2018).
[72]P. Pande, Y. Z. Liu, F. A. South, and S. A. Boppart, "Automated computational aberration correction method for broadband interferometric imaging techniques," Opt. Lett. **41**(14), 3324–3327 (2016).
[73]S. G. Adie, B. W. Graf, A. Ahmad, P. S. Carney, and S. A. Boppart, "Computational adaptive optics for broadband optical interferometric tomography of biological tissue," Proc. Natl. Acad. Sci. U. S. A. **109**(19), 7175–7180 (2012).

Published under an exclusive license by AIP Publishing